The Casimir energy between nanostructured gratings of arbitrary periodic profile

J. Lussange, R. Guérout, and A. Lambrecht

Laboratoire Kastler-Brossel, CNRS, ENS, UPMC, Case 74, F-75252 Paris, France

(Dated: October 26, 2012)

We study the lateral dependence of the Casimir energy for different corrugated gratings of arbitrary periodic profile. To this end we model the profiles as stacks of horizontal rectangular slices following the profiles' shape and evaluate numerically the Casimir energy between them for different relative lateral displacements of the two corrugated plates. We compare our results with predictions obtained within the proximity force approximation (PFA). At comparable separation of the corrugated plates and geometric parameters, we find a strong dependence of the Casimir energy on the shape of the corrugation profiles.

PACS numbers: 03.70.+k, 12.20.Ds, 42.50.Lc

I. INTRODUCTION

Two surfaces in quantum vacuum attract each other due to the fluctuations of the electromagnetic field prevailing in the vacuum state as predicted by H. Casimir in 1948 [1]. The Casimir force scales with the inverse of the fourth power of the surfaces' separation and can take on significant values between objects in the submicrometer range. Indeed, the dynamics of the electromagnetic field, including the vacuum field, strongly depends on its external boundary conditions, and the variation of its spectral density when the field is confined leads to differences in the vacuum radiation pressure resulting in a net force.

While the Casimir force is negligible at macroscopic scales it can become comparable to electric forces at submicron distances. In microelectromechanical systems (MEMS) it may produce sticking and adhesion of the system's components [2], but it may also be used to actuate the system [3, 4]. Modern measurement techniques have allowed for accurate determination and measurements of the Casimir force for different configurations and geometries. Casimir's original configuration of two flat parallel plates has been experimentally realized in [5]. Most of the measurements have however been performed between flat and spherical mirrors [4, 6–11], and some have employed cylinders [12, 13].

Deviations from the two plates geometry are often accounted for in calculations by using the proximity force approximation (PFA) which amounts to adding up local contributions to the Casimir force at different distances as if those were independent of each other [14]. Exact calculations have shown considerable deviations from PFA for the plane-sphere geometry [15, 16] and when nanostructured plates are used [17, 18]. In particular the normal Casimir force is affected by the gratings geometry, and the change cannot be reliably estimated within PFA as soon as the different length scales of the problem (corrugation period d, depth a and relative distance L) are of the same order. This is shown by the experiment reported in [19] for the interaction of a Au sphere with a Si grating with deep rectangular trenches. Exact calculations within a path integral approach of this geometry for perfectly reflecting plates [20] confirm the invalidity of

PFA but lead to too large a prediction for the force. Taking into account in the exact calculations the interplay between the surface geometry and the optical properties of the materials leads to good agreement between the experiment and theoretical predictions [17], as confirmed later on by another experiment using a shallow-trenched Si surface and comparing with independent theoretical calculations [18]. More recently these methods have been complemented by another approach based on a decomposition of the field onto the modes of the structures [21]. See also a recent review on Casimir forces in structured geometries by Rodriguez *et al* [22].

The use of nanostructured plates instead of flat surfaces also allows for the existence of lateral Casimir forces acting tangential to the surface and of Casimir torques. They arise when the translational invariance is broken, either due to the anisotropy of the material [23] or to surface structures [24]. Lateral Casimir forces were first calculated for scalar fields and perfect boundaries imprinted with one-dimensional (1D) sinusoidal corrugations [25, 26], where by 1D we mean corrugations following a single transverse direction. The case of electromagnetic fields and non-dissipative metallic surfaces was studied within the scattering approach in [27] and later on applied to Casimir-Polder interactions between a metallic nanostructure and Rb atoms [28]. The Casimir interaction involving single objects of elliptical shapes have been studied theoretically in [29–31] and experimentally in [13].

Experimental evidence of the lateral Casimir force was given for sinusoidal corrugations imprinted on a sphere and a plate, with corrugation periods d much smaller than the surfaces' separation L, and showed its sinusoidal variation with the plates' lateral displacement [32]. In this situation good agreement was found with calculations based on the PFA as the condition $d \ll L$ was satisfied. More recently, the same group has measured the lateral force for asymmetric sinusoidal profiles accompanied by exact calculations [33, 34] using the method developed in [17].

An interesting perspective for the lateral Casimir force lies in the realization of non-contact rack-and-pinion devices or ratchets [35–37] and of non-contact gears [38, 39]

which would allow for a force or torque transmission between corrugated surfaces without bringing them in direct contact with each other. Typical profiles studied in this context are sinusoidal.

In the present paper we study the Casimir energy between two nanostructured surfaces as a function of their lateral displacement from which the magnitude of the lateral force may be easily deduced. We use the scattering approach [40–42] to handle a variety of different periodic profiles. We present a detailed comparison of different profiles, such as circular, elliptical, triangular, trapezoidal and compare the Casimir energies they generate to those of the commonly used sinusoidal and rectangular profiles. Profiles with a base angle larger than for the rectangular profile generate stronger Casimir energies than profiles having a smaller base angle. While failing in general, we find the PFA to be a good approximation for the latter profiles displaced by half a corrugation period. Our results for circular and elliptical profiles can be applied to model the dispersive interaction between periodic arrays of nanowires or nanotubes [43–45].

II. SCATTERING FORMALISM

For parallel plates, the Casimir force may be written in terms of scalar reflection coefficients, but for non-planar surfaces the specular reflection coefficients must be replaced by general reflection operators that describe the non-specular diffraction by the surfaces [41]. In the case of two dielectric lamellar gratings, the Casimir interaction energy per unit area at zero temperature is given by [17]

$$E = \frac{\hbar}{(2\pi)^3} \iiint \mathrm{d}^2\mathbf{k}_\perp \mathrm{d}\xi \ln \det\left(\mathbf{1} - \mathcal{M}\right) \quad (1)$$
$$\mathcal{M} = \mathcal{R}_1 e^{-\kappa L}\mathcal{R}_2 e^{-\kappa L}$$

The Casimir energy is written in terms of reflection operators $\mathcal{R}_1$ and $\mathcal{R}_2$ which describe the diffraction by the two lamellar gratings. The operator $e^{-\kappa L}$ accounts for a one-way propagation along the distance L separating the two gratings, with $\kappa = \sqrt{\xi^2 + \mathbf{k}_\perp^2}$ the imaginary longitudinal wave-vector and $\mathbf{k}_\perp$ the transverse wave-vector, where all quantities are written at imaginary frequencies $\omega = i\xi$ after a Wick rotation. The operator $\mathcal{M}$ thus represents one round-trip propagation between the two surfaces.

Here we consider two dielectric lamellar gratings of arbitrary but symmetric profiles with a period d and corrugation depth a separated by a vacuum slit such as shown in Fig.1. In [17] a formalism has been developed to calculate the Casimir energy in this configuration for rectangular profiles. We generalize this approach to arbitrary profiles by dividing each corrugation line into K horizontal slices vertically stacked on each other. For a corrugation depth a, each slice is treated as a lamellar rectangular grating whose height along the $y-$axis is
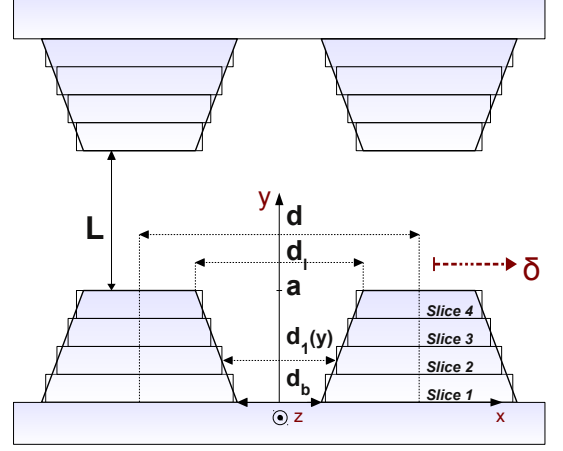

FIG. 1. Two nanostructured surfaces of arbitrary but symmetric profiles with a period d and corrugation depth a are divided into K vertical stacks of rectangular slices (here $K = 4$).

fixed at a/K and whose length along the $x-$axis is given by the profile's length at the level of the slice.

Let us first recall the main steps of the calculation for rectangular gratings separated by a vacuum slit. Because of time and z-invariance, we can write the electric and magnetic fields for $i = (x, y, z)$ such as :

$$E_i(x, y, z, t) = E_i(x, y)\exp(ik_z z - i\omega t) \quad (2)$$

$$H_i(x, y, z, t) = H_i(x, y)\exp(ik_z z - i\omega t). \quad (3)$$

In the following we will take $\mu_0 = \mu = 1$, and $c = 1$ in vacuum. We need to find the longitudinal components outside the corrugated region $(y > a)$ and within the transmitted region $(y \leqslant 0)$. In the case of two planar interfaces, we can write the $z-$components of the fields in the vacuum region as an incident and reflected field:

$$E_z(x, y) = I^e e^{ik_x x - ik_y y} + r^e e^{ik_x x + ik_y y} \quad (4)$$

$$H_z(x, y) = I^h e^{ik_x x - ik_y y} + r^h e^{ik_x x + ik_y y} \quad (5)$$

while in the material region, we can write the $z-$components of the fields as transmitted fields:

$$E_z(x, y) = t^e e^{ik_x x - ik_y' y} \quad (6)$$

$$H_z(x, y) = t^h e^{ik_x x - ik_y' y} \quad (7)$$

where $k_y^2 = \omega^2 - k_x^2 - k_z^2$ and $k_y'^2 = \epsilon\omega^2 - k_x^2 - k_z^2$ are the longitudinal wave-vectors in vacuum and inside the material. k_x, k_z are the components of the transverse wave-vector, ϵ is the material's frequency dependent permittivity. The coefficients $I^{e,h}$, $r^{e,h}$, $t^{e,h}$ are respectively the incident amplitudes and the Fresnel-Stokes reflection and transmission amplitudes in the (e, h)-basis of polarizations, which are defined by imposing $H_y = 0$ for the e-polarization and $E_y = 0$ for the h-polarization.

We may now generalize the above equations for gratings. Outside the corrugations ($y > a$), the fields are written as a Rayleigh expansion involving incident and reflected fields of order p and n respectively :

$$E_z(x,y)_{y>a} = I_p^e \exp(i\alpha_p x - i\beta_p^{(1)} y)$$
$$+ \sum_{n \in \mathbb{Z}} R_{np}^e \exp(i\alpha_n x + i\beta_n^{(1)} y) \quad (8)$$

$$H_z(x,y)_{y>a} = I_p^h \exp(i\alpha_p x - i\beta_p^{(1)} y)$$
$$+ \sum_{n \in \mathbb{Z}} R_{np}^h \exp(i\alpha_n x + i\beta_n^{(1)} y) \quad (9)$$

For the region inside the material ($y \leqslant 0$), the transmitted fields are given by :

$$E_z(x,y)_{y\leqslant 0} = \sum_{n \in \mathbb{Z}} T_{np}^e \exp(i\alpha_n x - i\beta_n^{(2)} y) \quad (10)$$

$$H_z(x,y)_{y\leqslant 0} = \sum_{n \in \mathbb{Z}} T_{np}^h \exp(i\alpha_n x - i\beta_n^{(2)} y), \quad (11)$$

where we have used:

$$\alpha_p = k_x + 2\pi p/d \quad (12)$$
$$\alpha_n = k_x + 2\pi n/d \quad (13)$$
$$\beta_p^{(1)2} = \omega^2 - k_z^2 - \alpha_p^2 \quad (14)$$
$$\beta_n^{(1)2} = \omega^2 - k_z^2 - \alpha_n^2 \quad (15)$$
$$\beta_n^{(2)2} = \epsilon\omega^2 - k_z^2 - \alpha_n^2. \quad (16)$$

I_p, R_{np}, and T_{np} are now the incidence, reflection, and transmission matrix elements respectively. $n = 0$ corresponds to a specular reflection. By symmetry, the other field components of the electric and magnetic fields can each be expressed through the z-components of both fields, following Maxwell's equations.

We now need to determine the reflection coefficients R_{np} of the rectangular corrugated gratings. To this aim we first rewrite Maxwell's equations inside the corrugated region $0 < y \leq a$ through the set of first-order differential equations $\partial_y \mathbf{F} = \mathbf{M}\mathbf{F}$, for $\mathbf{F}^\top = (E_x, E_z, H_x, H_z)$ and $\mathbf{M}$ a constant square matrix of dimension $8N + 4$. The solution for the fields is then of the form :

$$\mathbf{F}(y) = e^{\mathbf{M}y}\mathbf{F}(0) \quad (17)$$

with :

$$\mathbf{M} = \begin{pmatrix} 0 & 0 & \frac{-ik_z\alpha_n}{\epsilon\omega} & -i\frac{\epsilon\omega^2-\alpha_n^2}{\epsilon\omega} \\ 0 & 0 & i\frac{\epsilon\omega^2-k_z^2}{\epsilon\omega} & \frac{ik_z\alpha_n}{\epsilon\omega} \\ \frac{ik_z\alpha_n}{\omega} & i\frac{\epsilon\omega^2-\alpha_n^2}{\omega} & 0 & 0 \\ -i\frac{\epsilon\omega^2-k_z^2}{\omega} & \frac{-ik_z\alpha_n}{\omega} & 0 & 0 \end{pmatrix} (18)$$

where the elements appearing in matrix $\mathbf{M}$ are block matrices of dimension $2N + 1$. We can write the fields inside the corrugation region and match them through continuity relations for each E_x, E_z, H_x, H_z, with equation (17),

at boundary $y = a$ for $y > a$, and at boundary $y = 0$ for $y \leqslant 0$. This allows to find the vectors $\mathbf{F}(a)$ and $\mathbf{F}(0)$, which can be written as a product of a matrix and the vector of variables X :

$$\mathbf{F}(a) = TX + Y \quad \text{and} \quad \mathbf{F}(0) = SX \quad (19)$$

with $X^T = (R_{np}^e, R_{np}^h, T_{np}^e, T_{np}^h, \ldots)$, and Y being the variable-independent term including the polarization of the incident waves, since we must take into account the two polarizations, e and h independently: $I_p^{(e)} = 1$ and $I_p^{(h)} = 0$ for electric waves ($H_z = 0$), and $I_p^{(e)} = 0$ and $I_p^{(h)} = 1$ for magnetic waves ($E_z = 0$). Y hence characterizes the two separate solutions for e- and h-waves. The solution is then of the form:

$$X = (e^{\mathbf{M}a}S - T)Y. \quad (20)$$

We have :

$$X\left(I_p^{(e)} = 1, I_p^{(h)} = 0\right) = \begin{pmatrix} R_{np}^{(e,e)} \\ R_{np}^{(h,e)} \\ \vdots \end{pmatrix} \quad (21)$$

$$X\left(I_p^{(e)} = 0, I_p^{(h)} = 1\right) = \begin{pmatrix} R_{np}^{(e,h)} \\ R_{np}^{(h,h)} \\ \vdots \end{pmatrix} \quad (22)$$

so that we obtain the reflection matrix for each grating:

$$R(\omega) = \begin{pmatrix} R_{np}^{(e,e)} & R_{np}^{(e,h)} \\ R_{np}^{(h,e)} & R_{np}^{(h,h)} \end{pmatrix} \quad (23)$$

After making use of Cauchy's argument principle and normalizing the frequency by c, we arrive to the exact expression of the Casimir energy between the two gratings on a unit cell of period d and unit length in the y-direction, with $R_1(i\xi)$ and $R_2(i\xi)$:

$$E = \frac{\hbar dc}{8\pi^3} \int_{\mathbb{R}^{+*}} d\xi \int_{\mathbb{R}} dk_z \int_{-\pi/d}^{\pi/d} dk_x$$

$$\times \ln\det[\mathbf{1} - R_1(i\xi)e^{-\mathcal{K}L}R_2(i\xi)e^{-\mathcal{K}L}] \quad (24)$$

with $\mathcal{K} = \text{diag}(\sqrt{\xi^2 + k_y^2 + [k_x + (2m\pi/d)]^2})$ and $m = -N, \ldots, +N$. For the sake of clarity we have explicitly re-introduced the speed of light c here.

III. ARBITRARY PROFILES

We will now consider gratings of arbitrary symmetric profiles. The difference with the rectangular gratings appears in the parameter d_1, which will now depend on y. Arbitrary profiles defined by $d_1(y)$ can be divided into K slices, each of rectangular shape, as described in Fig.
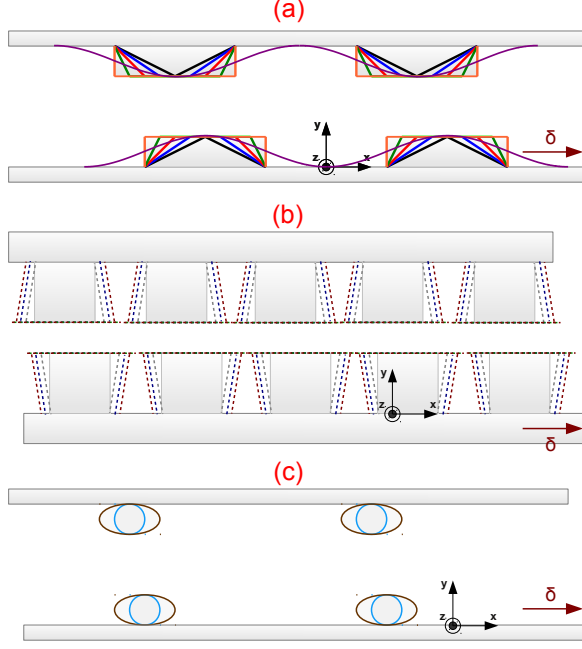
FIG. 2. Two-dimensional perspective on the different considered periodic gratings. (a) and (c) are at the same scale, whereas the scale of (b) has been increased by a factor two.

1. For each slice (i), the spacing between the corrugation ridges is $d_1^{(i)}$ and the former scattering formalism for rectangular corrugations can be applied. More specifically, a differential equation $\partial_y \mathbf{F} = \mathbf{M}^{(i)} \mathbf{F}$ akin to equation (17) can be solved within each slice (i) to relate the fields at boundary $y = i\frac{a}{K}$ and $y = (i+1)\frac{a}{K}$.

In a similar way than for the case $K = 1$ above, the field at $y = a$ is thus related to the field at $y = 0$ via the relation :

$$\mathbf{F}(a) = \left[\prod_{i=K}^{1} e^{\mathbf{M}^{(i)} \frac{a}{K}} \right] \mathbf{F}(0) \qquad (25)$$

where the product $\prod$ runs from $i = K$ to $i = 1$.

Hence a correct parametrization of the quantity d_1 as a function of y allows one to generate arbitrary symmetric profiles for the corrugations. The profiles that we will study as examples in the following are shown on Fig. 2 as cross sections while on Fig. 3 the grating structure becomes more apparent. Triangular profiles with $d_l = d$ as seen on Fig. 2a and Fig. 3 are generated by the function $d_1(y) = \frac{d}{a}y$, sinusoidal profiles by $d_1(y) = (d/\pi) \arccos[1 - (2y/a)]$. We also study two types of trapezoidal profiles, having a base angle smaller than $90°$ (Fig. 2a) on the one hand, and having a base angle larger than $90°$ (Fig. 2b) on the other hand. They are characterized by $d_b < d_l$ and $d_b > d_l$ respectively and are both generated by the function $d_1(y) = (d_l - d_b)y/a + d_b$. Ellipsoid profiles along the x- or y-axis are generated by
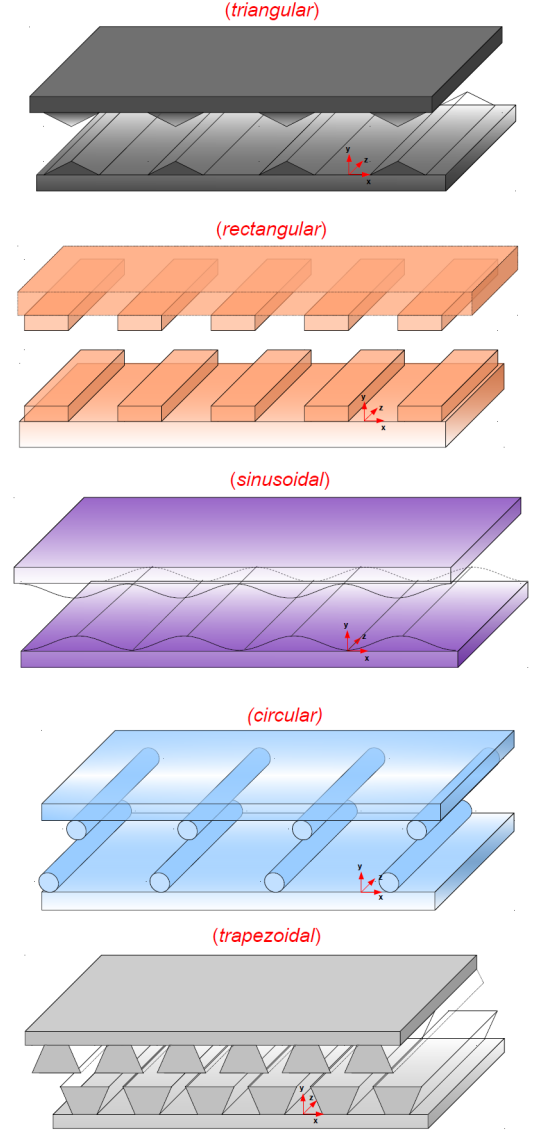

FIG. 3. Three-dimensional perspective on the triangular, rectangular, sinusoidal, circular, and trapezoidal periodic profiles shown in Fig. 2. The profiles are here represented at the same scale.

$d_1(y) = d - \frac{2R}{r}\sqrt{r^2 - (y - Y)^2}$ (Fig. 2c) and $d_1(y) = d - \frac{2r}{R}\sqrt{R^2 - (y - Y)^2}$ respectively, for R and r being the major and minor axes of the ellipse, and Y being the value of the y-coordinate of the ellipse center. Circular periodic profiles are also generated by these expressions (as seen on Fig. 2c and Fig. 3), with $R = r$ being the radius in the xy-plane. Note that what we call for example a circular or elliptical periodic profile is in fact a geometry where equally spaced parallel wires of circular or elliptical cross-section cover the surfaces, as shown on Fig. 3.

Obviously a given profile will be better fitted for greater numbers of slices K. The number of slices thus determines the accuracy of the overall model. Fig. 4
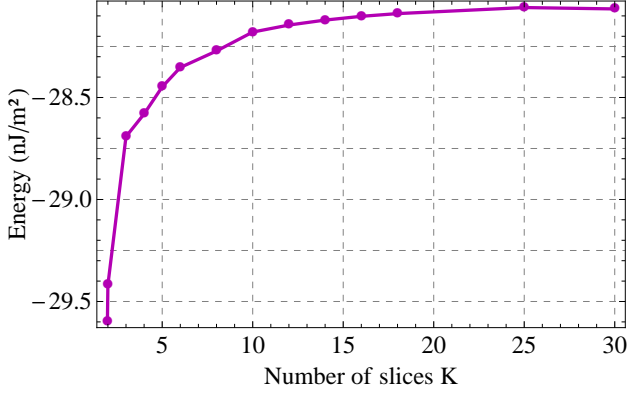
FIG. 4. Dependence of the Casimir energy on the number of slices K for two triangular gratings, with $L = 100$ nm, $d = 400$ nm, $a = 50$ nm, and $d_1(y) = 4y + 200$.
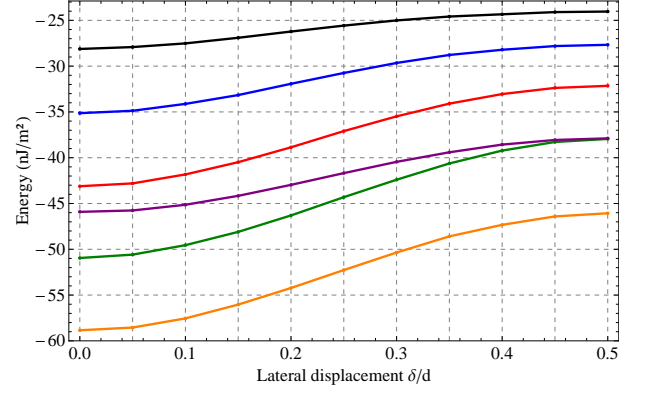

FIG. 5. Dependence of the Casimir energy on the lateral displacement between two corrugated periodic profiles of intrinsic silicon for $L = 100$ nm, $K = 20$, $d = 400$ nm, $a = 50$ nm, and from top to bottom, $d_1 = 4y + 200$ (triangular in black), $d_1 = 3y + 200$ (blue), $d_1 = 2y + 200$ (red), sinusoidal profile (purple), $d_1 = y + 200$ (green) and $d_1 = 200$ (rectangular in orange). The sinusoidal profile is plotted for the same parameters, except $d_1 = (d/\pi)\arccos[1 - (2y/a)]$.

shows the Casimir energy as a function of the number of slices for two triangular profiles at a distance $L = 100$ nm, for a grating period $d = 400$ nm, corrugation depth $a = 50$ nm, and distance between the ridges $d_1(y) = 4y + 200$. For this example, convergence sets in for $K \approx 20$.

In the following we will also compare the results of the scattering theory presented here with the proximity force approximation [14]. The PFA comes from the weighted sum of the planar normal contributions $E_{PP}(L)$ depending on the local distances L within each period, and hence also on the lateral displacement δ between the gratings. If we express the shapes of the arbitrary periodic gratings in an analytical form such as $y = f(x, \delta)$ for the lower grating and $y = L + 2a - f(x, \delta = 0)$ for the upper grating in the xy-plane shown on Fig. 1, we can then define the function $h(x, \delta) = L + 2a - f(x, \delta = 0) - f(x, \delta)$ in order to express the local distance of separation between the two profiles. Dividing the period d in a number $N \to \infty$ of intervals of individual widths $d/N \to 0$, we then obtain a general expression of the Casimir energy in the PFA for arbitrary gratings as a function of lateral displacement δ :

$$E^{PFA}(L, \delta) = \frac{1}{d} \int_0^d E_{PP}\left(h(x, \delta)\right) dx \qquad (26)$$

$$= \frac{1}{N} \sum_{i=1}^{N} E_{PP}\left(L = h\left(x = i\frac{d}{N}, \delta\right)\right)$$

IV. CASIMIR ENERGY FOR ARBITRARY PERIODIC GRATINGS

We now evaluate numerically the Casimir energy for several types of profiles as a function of the surfaces' relative lateral displacement δ. The material chosen for these profiles is intrinsic silicon, which can be described

by a Drude-Lorentz function [46]

$$\epsilon(i\xi) = \epsilon_\infty + \frac{(\epsilon_0 - \epsilon_\infty)\omega_0^2}{\omega^2 + \omega_0^2} \qquad (27)$$

The numerical values are determined by realizing that at low-frequencies the dielectric function of intrinsic silicon approaches the constant value $\epsilon_0 = 11.87$ while with increasing frequency it is nearly constant and falls off only for high frequencies above a cut-off frequency $\omega_0 \approx 6.6 \cdot 10^{15}$ rad/s. For high frequencies it reaches the asymptotic value $\epsilon_\infty = 1.035$ [47].

We first study the transition from triangular over trapezoidal to rectangular profiles, such as sketched by the colored shapes of Fig. 2a. Those profiles are parametrized from top to bottom by $d_1(y) = 4y + 200$ (triangular: black), $d_1(y) = 3y + 200$ (trapezoidal: blue), $d_1(y) = 2y + 200$ (trapezoidal: red), $d_1(y) = y + 200$ (trapezoidal: green), and $d_1(y) = 200$ (rectangular: orange) respectively. For these profiles the top distance d_l decreases successively from $d_l = d = 400$ nm to $d_l = d_b = 200$ nm by steps of 50 nm. The different Casimir energies for $L = 100$ nm, $d = 400$ nm, $a = 50$ nm, and a number of slices $K = 20$, are depicted in Fig. 5. Clearly the Casimir energy increases as d_l decreases, and this is especially true at $\delta = d/2$, meaning that both the Casimir energy and its modulation over lateral displacement are larger for smaller d_l, i.e. for rectangular gratings and smaller for larger d_l such as triangular profiles. Note also the behavior of the sinusoidal profile at $\delta = d/2$, which shows that such profiles are much less sensitive to lateral displacement than triangular profiles or rectangular gratings.

On Fig. 6 we show a comparison between the exact results from the scattering formalism (solid lines) and the predictions from PFA (dashed lines) for the triangular,
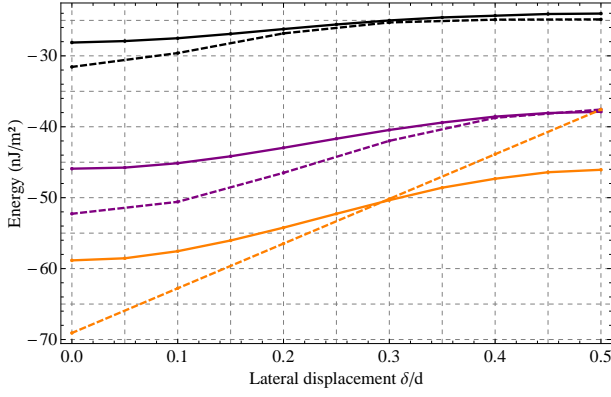
FIG. 6. Comparison between the exact results from scattering theory (solid lines) and PFA predictions (dashed lines) for the triangular (black), sinusoidal (purple), and rectangular (orange) profiles of Fig. 5.
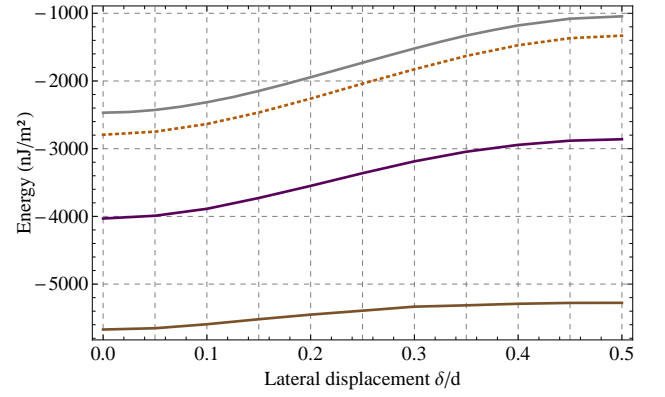

FIG. 7. Dependence of the Casimir energy on the relative lateral displacement of two trapezoidal periodic profiles of intrinsic silicon for $L = 20$ nm, $K = 20$, $d = 100$ nm, $a = 50$ nm, and, from top to bottom, $d_1 = -0.5y + 85$ (grey), $d_1 = -0.5y + 65$ (deep purple), $d_1 = -0.5y + 45$ (brown). This is compared to rectangular profiles with $d_1 = d_l = 60$ nm (orange dotted line). While we varied the spacing between the corrugations d_1, the grating period d was kept constant.
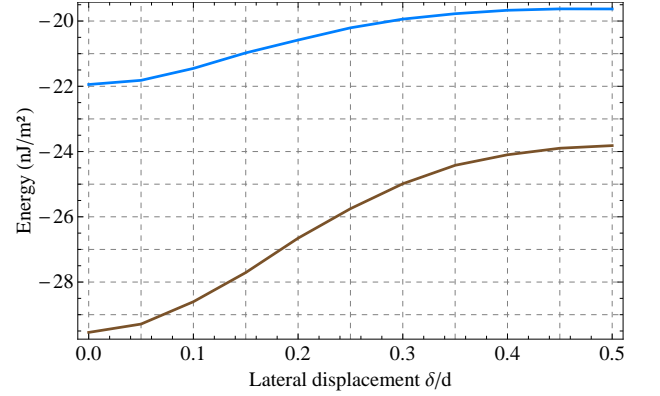

FIG. 8. Dependence of the Casimir energy on the relative lateral displacement between two periodic profiles shaped as circular (light blue) and ellipsoid (brown) from top to bottom for $L = 100$ nm, $K = 15$, $d = 400$ nm, $a = 50$ nm, and $d_1 = 400 - 2\sqrt{50y - y^2}$ (circular with $R = r = Y = 25$ nm), and $d_1 = 400 - 4\sqrt{50y - y^2}$ (ellipsoid with $r = Y = 25$ nm and $R = 50$ nm).

sinusoidal, and rectangular profiles (from top to bottom). Regardless of the considered profile, the PFA fails to correctly describe the situation of no lateral displacement $\delta = 0$. The error ratio $E_{\mathrm{PFA}} - E_{\mathrm{scattering}}/E_{\mathrm{PFA}}$ there is approximately equal to 11% for triangular, 12% for sinusoidal, and 15% for rectangular gratings. As one shifts δ to half-a-period $\delta = d/2$, the relative error for rectangular gratings passes through zero to reach basically the same value of opposite sign at $\delta = d/2$. For rectangular gratings PFA thus underestimates the Casimir energy when corrugation maxima face maxima and overestimates it when maxima face minima. However, PFA turns out to give valid predictions for triangular and sinusoidal gratings when they have a relative lateral shift of half a period. This is due to the fact that, unlike for rectangular gratings, in this situation the two triangular or sinusoidal profiles become parallel to each other.

We now study the particular case of trapezoidal profiles for which $d_b > d_l$, with a base angle larger than rectangular gratings. We illustrate the results on Fig. 7 for $L = 20$ nm, $d = 100$ nm, $a = 50$ nm, and a number of slices $K = 20$. The profiles are enlarged on the top while keeping the base constant via a parametrization $d_1 = -0.5y + 85$ (grey), $d_1 = -0.5y + 65$ (deep purple), $d_1 = -0.5y + 45$ (brown) from top to bottom. The dotted orange line corresponds to the Casimir energy between rectangular gratings with $d_1 = d_l = 60$ nm so that the corrugations are as wide as the top of the trapezoidal profile $d_1 = 85 - y/2$. The difference in the Casimir energies associated with the rectangular profiles and the trapezoidal profiles, which have the same surface exposed in the near field, implies the existence of highly non-trivial mode contributions in the vicinity of the bases of the trapezoidal gratings.

Finally we consider the Casimir interaction between two elliptical and two circular profiles, as shown in Fig. 8, for $L = 100$ nm, $d = 400$ nm, $a = 50$ nm, and a number of slices $K = 15$. The elliptical profile (lower curve in brown) has a major axis $R = 50$ nm along x, a minor

axis $r = 25$ nm, and its origin at $y = Y = 25$ nm, so that $d_1(y) = 400 - 4\sqrt{50y - y^2}$. The circular profile (upper curve in blue) has a radius $R = 25$ nm and its center at $y = Y = 25$ nm, such that $d_1 = 400 - 2\sqrt{50y - y^2}$. The Casimir energy increases with the ratio R/r. This is again especially true at $\delta = d/2$. We may also note that compared to the profiles studied in Fig. 5, the energy varies much more rapidly over δ for the ellipsoid and circular profiles. This could be a consequence of the concave nature of these shapes for $y < Y$ and could potentially affect the lateral Casimir force applications mentioned earlier [35–39]. At fixed geometrical parameters and distances, the Casimir energy is overall much smaller

for these profiles than for the triangular and trapezoidal shapes discussed before.

V. CONCLUSION

We have studied the dependence of the Casimir energy on the lateral displacement for different arbitrary periodic gratings, ranging from triangular and sinusoidal profiles, to trapezoidal, circular and ellipsoid shapes. Concerning the trapezoidal profiles, we find that at the same distance L, grating period d, and corrugation depth a, the Casimir energy and its lateral modulation increase from triangular profiles over rectangular ones to those whose base angle is larger than $90°$. This seems a consequence of the fact that for a given surface, the Casimir energy increases when the exposed surfaces in near-field is increased. Profiles with large base angles or at least rect-angular profiles seem therefore more promising for lateral Casimir force, Casimir torque or other non-contact devices [35–39] than sinusoidal or triangular profiles. However, the exposed surface in near-field is not sufficient to estimate reliably the magnitude of the Casimir interaction even for small corrugation depth ($a < L$), as shown by the comparison of the Casimir energies between rectangular gratings and large base trapezoidal profiles. While failing to describe the Casimir interaction correctly in general, interestingly PFA gives valid predictions for sinusoidal and triangular gratings when they are relatively displaced by half a grating period. An interesting topic to further investigate would be to parametrize the profiles such that the lateral displacement δ also depends on y, thus generating asymmetric profiles [34].

[1] C. H.B.G., Proc. kon. Ned. Ak. Wet **51**, 793 (1948).
[2] E. Buks and M. Roukes, Europhysics Letters **54**, 220 (2001).
[3] H. B. Chan, V. A. Aksyuk, R. N. Kleiman, D. J. Bishop, and F. Capasso, Science **291**, 1941 (2001).
[4] H. B. Chan, V. A. Aksyuk, R. N. Kleiman, D. J. Bishop, and F. Capasso, Phys. Rev. Lett. **87**, 211801 (2001).
[5] G. Bressi, G. Carugno, R. Onofrio, and G. Ruoso, Phys. Rev. Lett. **88**, 041804 (2002).
[6] S. K. Lamoreaux, Phys. Rev. Lett. **78**, 5 (1997).
[7] U. Mohideen and A. Roy, Physical Rewiev Letters **81**, 4549 (1998).
[8] R. S. Decca, D. López, E. Fischbach, and D. E. Krause, Phys. Rev. Lett. **91**, 050402 (2003).
[9] M. Lisanti, D. Iannuzzi, and F. Capasso, Proceedings of the National Academy of Sciences of the United States of America **102**, 11989 (2005).
[10] G. Jourdan, A. Lambrecht, F. Comin, and J. Chevrier, EPL **85**, 31001 (2009).
[11] S. T. A. L. G. Torricelli, I. Pirozhenko and C. Binns, EPL **93**, 51001 (2011).
[12] T. Ederth, Phys. Rev. A **62**, 062104 (2000).
[13] R. S. Decca, E. Fischbach, G. L. Klimchitskaya, D. E. Krause, D. López, and V. M. Mostepanenko, Phys. Rev. A **84**, 042502 (2011).
[14] B. V. Derjaguin, Kolloid-Zeitschrift **69**, 155 (1934).
[15] A. Canaguier-Durand, P. A. M. Neto, I. Cavero-Pelaez, A. Lambrecht, and S. Reynaud, Physical Review Letters **102**, 230404 (2009).
[16] A. L. A. Canaguier-Durand, P.A. Maia Neto and S. Reynaud, Phys. Rev. Lett. **104**, 040403 (2010).
[17] A. Lambrecht and V. N. Marachevsky, Physical Review Letters **101**, 160403 (2008).
[18] Y. Bao, R. Guérout, J. Lussange, A. Lambrecht, R. A. Cirelli, F. Klemens, W. M. Mansfield, C. S. Pai, and H. B. Chan, Phys. Rev. Lett. **105**, 250402 (2010).
[19] H. B. Chan, Y. Bao, J. Zou, R. A. Cirelli, F. Klemens, W. M. Mansfield, and C. S. Pai, Phys. Rev. Lett. **101**, 030401 (2008).
[20] R. Büscher and T. Emig, Phys. Rev. A **69**, 062101 (2004).
[21] P. S. Davids, F. Intravaia, F. S. S. Rosa, and D. A. R. Dalvit, Phys. Rev. A **82**, 062111 (2010).
[22] A. W. Rodriguez, F. Capasso, and S. G. Johnson, Nature Photonics **5**, 211 (2011).
[23] J. N. Munday, D. Iannuzzi, Y. Barash, and F. Capasso, Phys. Rev. A **71**, 042102 (2005).
[24] R. B. Rodrigues, P. A. M. Neto, A. Lambrecht, and S. Reynaud, EPL (Europhysics Letters) **76**, 822 (2006).
[25] R. Golestanian and M. Kardar, Phys. Rev. Lett. **78**, 3421 (1997).
[26] T. Emig, A. Hanke, R. Golestanian, and M. Kardar, Phys. Rev. Lett. **87**, 260402 (2001).
[27] R. B. Rodrigues, P. A. M. Neto, A. Lambrecht, and S. Reynaud, Phys. Rev. Lett. **96**, 100402 (2006).
[28] D. A. R. Dalvit, P. A. M. Neto, A. Lambrecht, and S. Reynaud, Phys. Rev. Lett. **100**, 040405 (2008).
[29] B. E. Sernelius and C. E. Román-Velázquez, Phys. Rev. A **78**, 032111 (2008).
[30] T. Emig, N. Graham, R. L. Jaffe, and M. Kardar, Phys. Rev. A **79**, 054901 (2009).
[31] M. Levin, A. P. McCauley, A. W. Rodriguez, M. T. H. Reid, and S. G. Johnson, Phys. Rev. Lett. **105**, 090403 (2010).
[32] F. Chen, U. Mohideen, G. L. Klimchitskaya, and V. M. Mostepanenko, Phys. Rev. Lett. **88**, 101801 (2002).
[33] H.-C. Chiu, G. L. Klimchitskaya, V. N. Marachevsky, V. M. Mostepanenko, and U. Mohideen, Phys. Rev. B **80**, 121402 (2009).
[34] H.-C. Chiu, G. L. Klimchitskaya, V. N. Marachevsky, V. M. Mostepanenko, and U. Mohideen, Phys. Rev. B **81**, 115417 (2010).
[35] A. Ashourvan, M. Miri, and R. Golestanian, Phys. Rev. Lett. **98**, 140801 (2007).
[36] T. Emig, Phys. Rev. Lett. **98**, 160801 (2007).
[37] M. Miri, V. Nekouie, and R. Golestanian, Phys. Rev. E **81**, 016104 (2010).
[38] I. Cavero-Peláez, K. A. Milton, P. Parashar, and K. V. Shajesh, Phys. Rev. D **78**, 065018 (2008).
[39] I. Cavero-Peláez, K. A. Milton, P. Parashar, and K. V. Shajesh, Phys. Rev. D **78**, 065019 (2008).

[40] M. Jaekel and S. Reynaud, Journal de Physique I **1**, 1395 (1991).

[41] A. Lambrecht, P. Neto, and S. Reynaud, New Journal of Physics **8**, 243 (2006).

[42] T. Emig, N. Graham, R. L. Jaffe, and M. Kardar, Phys. Rev. Lett. **99**, 170403 (2007).

[43] Y. Qin, R. Yang, and Z. L. Wang, The Journal of Physical Chemistry C **112**, 18734 (2008).

[44] X. Sheng, Y. Ding, Y. Wei, H. Fang, Y. Shen, A. K. Sood, D. L. Polla, and L. Wang Zhong, J. Am. Chem. Soc. **19**, 131 (2009).

[45] F. M. C. S. Soman P, Darnell M, J Nanosci Nanotechnol. **11**, 6880 (2011).

[46] L. Bergström, Adv. in Colloid and Interface Science **70**, 125 (1997).

[47] I. Pirozhenko and A. Lambrecht, Phys. Rev. A **77**, 013811 (2008).